NANO LETTERS

2007
Vol. 7, No. 9
2552−2558

Ultrafast Electron Microscopy (UEM): Four-Dimensional Imaging and Diffraction of Nanostructures during Phase Transitions

Vladimir A. Lobastov, Jonas Weissenrieder, Jau Tang, and Ahmed H. Zewail*

Physical Biology Center for Ultrafast Science and Technology, Arthur Amos Noyes Laboratory of Chemical Physics, California Institute of Technology, Pasadena, California 91125

Received June 5, 2007

ABSTRACT

Four-dimensional (4D) imaging during structural changes are reported here using ultrafast electron microscopy (UEM). For nanostructures, the phase transition in the strongly correlated material vanadium dioxide is our case study. The transition is initiated and probed in situ, in the microscope, by a femtosecond near-infrared and electron pulses (at 120 keV). Real-space imaging and Fourier-space diffraction patterns show that the transition from the monoclinic ($P2_1/c$) to tetragonal ($P4_2/mnm$) structure is induced in 3 ± 1 ps, but there exists a nonequilibrium (metastable) structure whose nature is determined by electronic, carrier-induced, structural changes. For the particles studied, the subsequent recovery occurs in about 1 ns. Because of the selectivity of excitation from the $3d_{||}$-band, and the relatively low fluence used, these results show the critical role of carriers in weakening the V^{4+}–V^{4+} bonding in the monoclinic phase and the origin of the nonequilibrium phase. A theoretical two-dimensional (2D) diffusion model for nanoscale materials is presented, and its results account for the observed behavior.

Ultrafast electron microscopy (UEM) and diffraction have been developed in this laboratory to study structural dynamics with atomic-scale spatial and temporal resolutions.[1−6] The ability to image in real space provides the means to visualize nanometer-scale structures and to selectively record diffraction from areas of interest. In a previous publication, we reported an UEM study of the phase transition in vanadium dioxide (VO_2) materials.[4] It was shown that the structural transition is sensitive to the joint interaction of the femtosecond light and electron pulses and that structural change for particles of our specimen occurs in 3 ± 1 ps. In these studies, we employed pulses in the single-electron regime, definitely below the space charge limit, but separation between pulses was not sufficiently long to ensure reversibility of the change.

In this contribution, we report, using a "pulse picker" arrangement in our microscope, the dynamics of the structural transition during the change, from the low-temperature monoclinic (insulator or semiconductor) to the high-temperature tetragonal (metal, rutile) phase and over the time scale of structural recovery; henceforth, the tetragonal structure will be referred to as the rutile phase. The transition, which thermally occurs near 68 °C, is induced using near-infrared femtosecond pulses. Here, the direct, real-space images and diffraction patterns for this insulator to metal change and recovery are obtained with UEM. We discuss the nature of the ultrafast transition and the influence of nanoscale structures on the dynamics of recovery and compare with previous studies made using optical and X-ray probes.[7−12] A simple theoretical model is introduced in order to account for the observed nonexponential temporal behavior.

The UEM design has previously been described in detail.[4−6] Briefly, this microscope (UEM1) is operated using 120 fs frequency-doubled laser pulses (388 nm), which enter through a set of optical elements. The pulses are focused onto the cathode in order to generate electron packets by photoemission; the electron is accelerated to 120 keV ($\lambda_{\text{de Broglie}} = 3.349$ pm). A second femtosecond train of laser pulses (776 nm) is similarly directed toward the specimen for initiation of the process under study. The repetition rate of the laser pulses was controlled in the range from 80 MHz to 800 kHz by using a pulse picker, which contains a quartz Bragg cell. The light pulses were carefully steered by using a home-built computer-controlled mirror assembly and focused to a ~ 50 μm spot on both the sample and the photocathode. The precision of the alignment of electron and optical pulses are better than 10 μm.

Polycrystalline VO_2 thin film samples were grown by spin-coating a sol−gel[4,13] onto a freshly cleaved mica substrate. After the coating process, the film was heated to 350 K in air, followed by an annealing for 2 h at 875 K in a nitrogen environment. The VO_2 films were lifted off the mica

* Corresponding author. E-mail: zewail@caltech.edu.

10.1021/nl071341e CCC: $37.00
Published on Web 07/10/2007

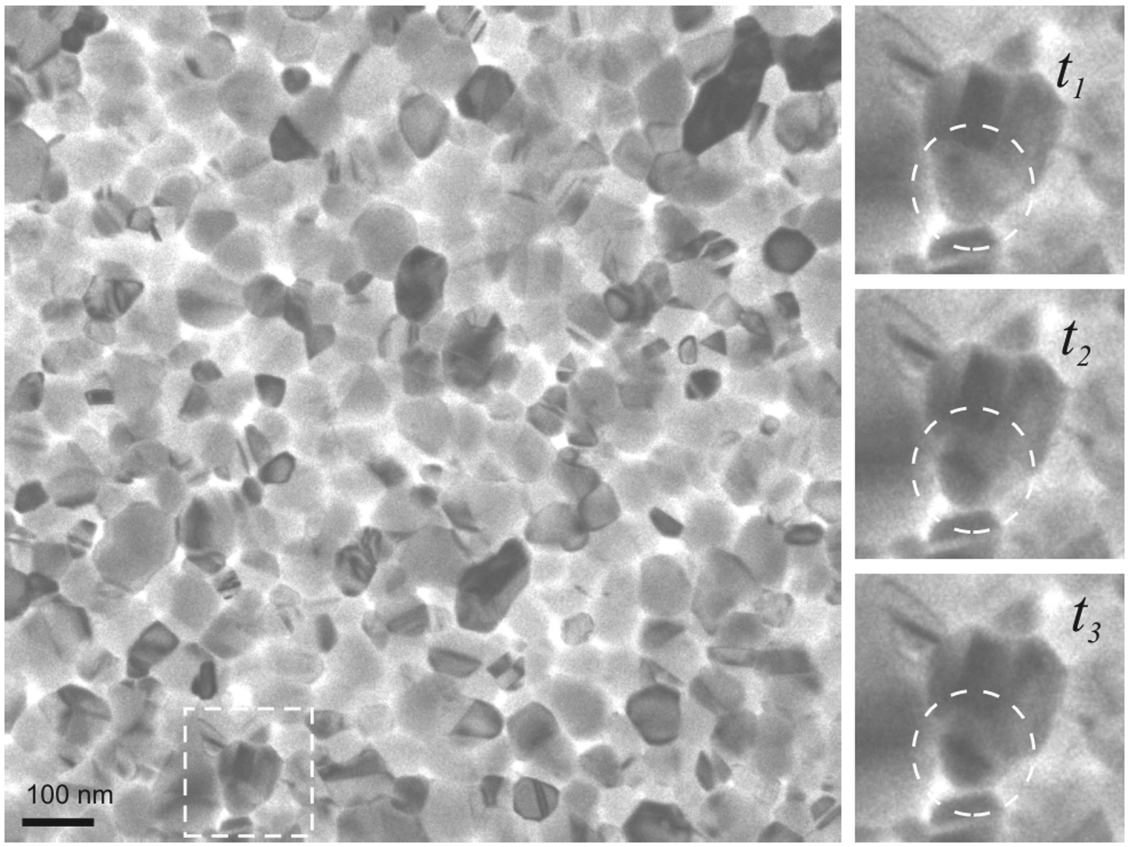

Figure 1. UEM real-space images of vanadium dioxide. The large image was taken at a magnification ×15 000 immediately after time zero. The three frames on the right show the temporal change of the zoomed in region, which is indicated by the square area in the large image. Selected frames are displayed for times t_1, t_2, and t_3 during and after the phase transition (0, 3, and 6 ps, respectively).

substrate in high-purity deionized water, placed onto a 300 mesh molybdenum grid, and then immediately inserted into the UEM for characterization.

Figure 1 displays typical real-space micrographs of the VO_2 material taken in the UEM mode and at different time delays. The full image in Figure 1 was taken immediately after time zero. Three frames are displayed for times t_1, t_2, and t_3 during the phase transition (0, 3, and 6 ps). The three frames on the right show the temporal change of the zoomed-in particle region, which is indicated by the square area in the full image. As can be seen in the images of the lower part of the grain (indicated in circles), changes occur on the time scale of the phase transition. The sample is polycrystalline, with the particles having a mean radius of 56 ± 21 nm, as shown below. The time-resolved real-space images support the conclusion from diffraction data (see below) that all particles are not involved in the phase transition; only a fraction of the grains switch the phase during the "pump−probe" cycle.

In Figure 2, we present typical selected-area transmission electron diffraction patterns. The lower left panel of the frame shown is a pattern from the more symmetric, high-temperature rutile phase (space group $P4_2/mnm$).[14] A simulated electron diffraction pattern for this phase is shown to the right (lower), and the agreement is satisfactory. The crystal structure projected along *b* onto the *ac* plane displays the vanadium atom in the center of the unit cell for the rutile; however, it is shifted half a unit cell in the *b* direction, as shown below.

Below the structural phase transition, the $V^{4+}(3d^1)$ ions dimerize along the rutile *c* direction and distort the lattice. The $V^{4+}-V^{4+}$ distance in the dimers is only 2.602 Å as compared to 2.856 Å in the rutile phase.[14] Furthermore, distortion of the VO_6 octahedra induces an antiferroelectric displacement of the V atoms perpendicular to the rutile *c* axis. As a result of the loss in symmetry and unit cell doubling in the rutile *c* direction, new diffraction peaks emerge, as can be seen in the upper left panel of the frame in Figure 2. The low-temperature phase is monoclinic (space group $P2_1/c$)[14] and the simulated diffraction pattern accurately predicts all peaks. The monoclinic *a* direction is parallel to the rutile *c* direction, and every second $V^{4+}-V^{4+}$ dimer should be viewed as shifted half a unit cell in the *b* direction.

The temporal changes of the structures, obtained in the microscope, are shown in Figures 2 and 3. The data in Figure 3 were obtained from angular integration of diffraction patterns at different laser-pump electron-probe time delays. The current diffraction measurements were performed at a repetition rate of 800 kHz with a pump fluence as low as ~0.1 mJ/cm^2. The sample temperature at a negative time delay, determined by the average pump power, was fine-tuned to the onset of the monoclinic−rutile phase transition. It is evident from the diffraction data that a rapid decrease in diffraction intensity of the peaks indexed $(10\bar{2})$ and $(30\bar{2})$

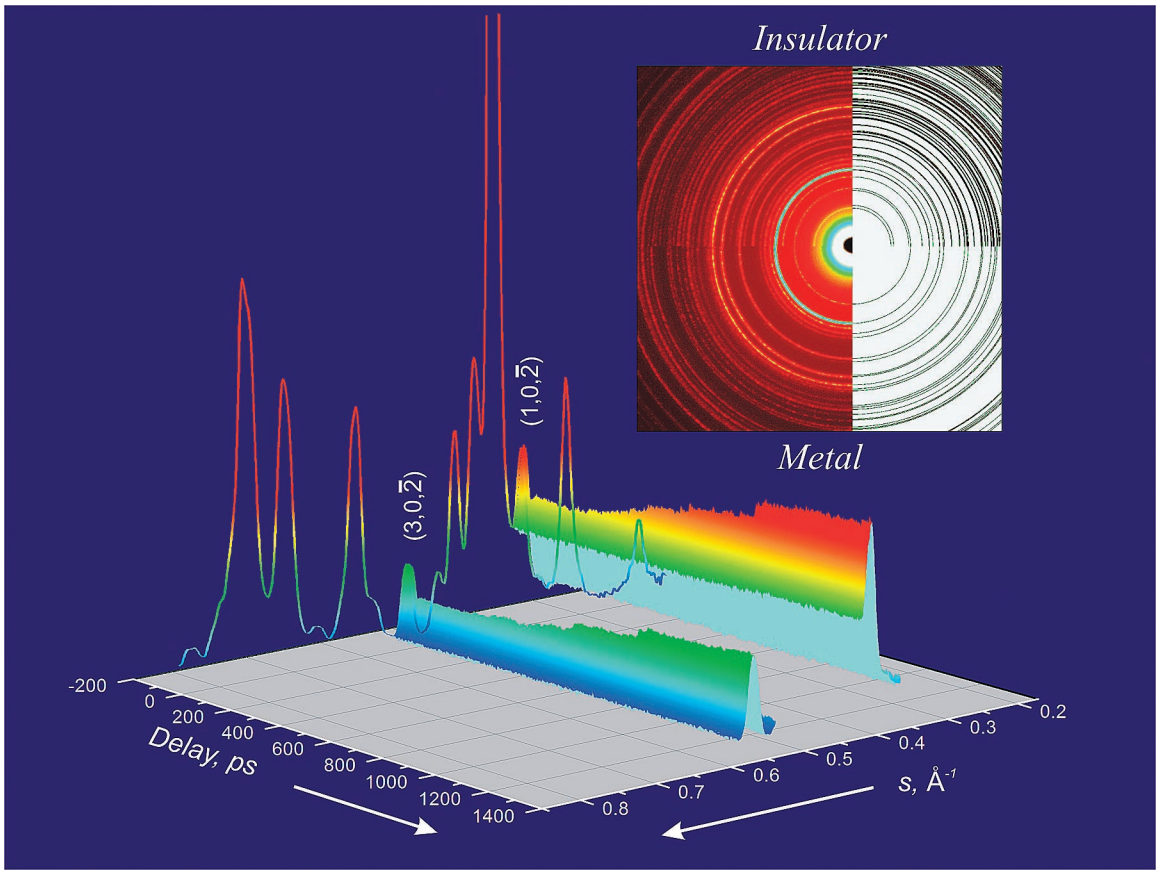

Figure 2. UEM diffraction patterns. Dynamics of angle-integrated patterns at different time delays and in *s*-space. Evolutions of the monoclinic phase-specific diffraction peaks (30$\bar{2}$) and (10$\bar{2}$) are shown. Frame inset shows a composite diffraction pattern of the two phases observed experimentally (left) and analyzed theoretically (right). The top half of the frame is for the monoclinic (insulator) phase and the bottom is for the tetragonal (metal) phase.

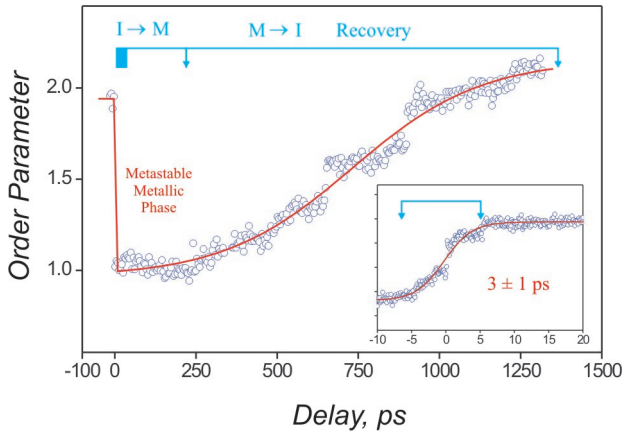

Figure 3. Temporal evolution of the structural order parameter. The order parameter is defined as the integrated intensity of the diffraction peak (30$\bar{2}$) for different temporal frames. This peak is characteristic of the monoclinic phase only, and for the pure tetragonal phase the intensity of the peak is zero. The change in value from nearly 2 to 1 is because not all nanocrystallites are switched (see text). Three temporal regions are highlighted: ultrafast insulator-to-metal, metastable phase, and diffusive recovery. The inset shows the ultrafast change of phase transition.

occurs near zero time delay. The inset shows in further detail the integrated intensity of (30$\bar{2}$) as a function of delay time. The initial drop represents the ultrafast phase transition and can be correlated with the rise of 3 ± 1 ps.[4] This decrease in diffraction intensity of (10$\bar{2}$) and (30$\bar{2}$) is expected as the crystal structure changes from the monoclinic to rutile phase; we note that the notation of indices here[14] are somewhat different from those in reference,[4] but for the diffraction peaks the unique direction of the *b* axis remains.

The true nature of the time dependence was carefully verified by varying the following experimental conditions: repositioning of the delay line, recording of patterns at different step lengths and integration times, and the variation of the laser repetition rate. All measurements were consistent with the change being from the low-temperature to the high-temperature phase. From the measured change in diffraction intensity, we conclude that the entire specimen does not undergo the phase transition with a significant fraction of the particles remaining in the monoclinic phase throughout the change. As such, the definition of a fluence "threshold" is appropriate only if all members of the ensemble are switched. The recovery to the monoclinic phase by the fraction of the sample that went through the phase transition to the rutile phase occurs in about 1 ns (Figure 3). This dynamics is observed here because the pulse energy is 100 times higher than that reposted in ref 4, and the separation between pulses is sufficiently long (1.25 μs).

The phase transition in VO_2 has been extensively studied by a wide range of experimental techniques, beginning with measurements of heat capacity as a function of temperature

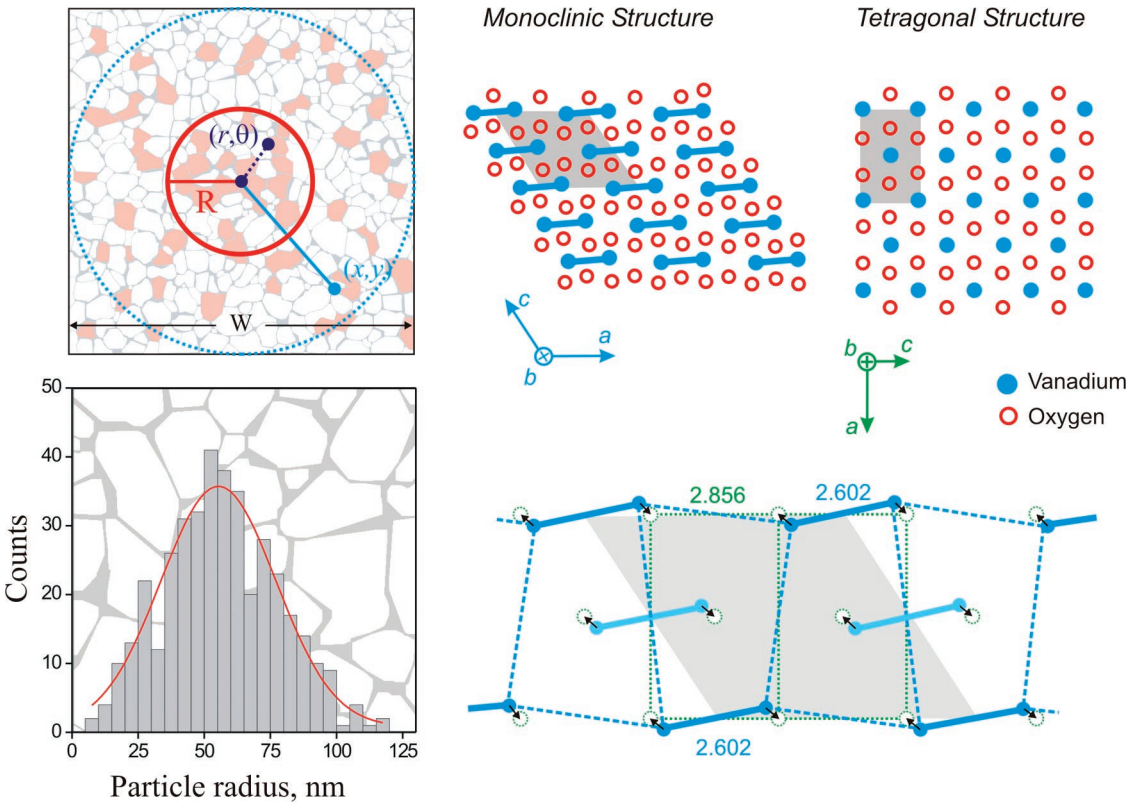

Figure 4. Macroscopic and microscopic structures. Left (top) panel shows the VO_2 sample morphology and superimposed are the parameters definition for our theoretical model; the left (bottom) panel shows the size distribution of nanocrystals with the Gaussian distribution indicated in red. Right-hand panels display the microscopic structures of the two phases projected on the *ac*-plane, with the corresponding unit cells in gray. The right (bottom) panel presents vanadium structural skeleton overlapped for both phases with arrows indicating the direction of nuclear motions. The unit cell for monoclinic is in gray, for the tetragonal in dotted green, and the V−V pairs in lighter colors are shifted half a unit cell in the *b* axis direction.

that identify the transition as a first order.[15−17] A majority of the studies use optical pump−probe reflectivity and transmission[7,9,11,12] measurements at different wavelengths and pulse lengths.[9] The other class of studies had focused on the change in local electronic structure using time-resolved X-ray absorption spectroscopy[7,9] or the structural phase transition using time-resolved vibrational phonon analysis[10] and X-ray diffraction.[9] In these studies, the phase transition of particles (or films) had not been imaged in real space, which can only be made using microscopy with the appropriate spatial and temporal resolutions.

The UEM results reported here highlights four new findings. First, the study represents the first combined time-resolved (real-space) image and (Fourier-space) diffraction mapping of a structural change before, during, and after the transition. Combined image-diffraction studies are important for understanding the nature of the phase transition, a correlated macroscopic phenomenon, as they establish the interconnection between macroscopic domains (morphology, grain structure, particle size) and microscopic (unit cell properties and lattice symmetry) structures and their temporal evolution. Moreover, time-resolved images and patterns originate from *exactly* the same investigated area of the material and, whether the data are collected in a real (imaging) or Fourier (diffraction) space, the choice is determined only by the post-specimen settings of the objective lens. As a result, real-space imaging provides the dynamics of the overall macroscopic behavior of the specimen, including particle size analysis and variation of dynamics in selected regions of interest, while selected-area diffraction provides the evolution of the microscopic order parameter, which reflects changes of unit cell and symmetry, both from the same region.

Second, the distribution of particle size, nature of excitation, and extent of the phase transition are interconnected. As mentioned above, from the images and diffraction, not all crystallites undergo structural phase transition upon near-IR pulse illumination. To address this issue, we investigated the particle size distribution of the material in the images taken. As shown in Figure 4, the distribution is centered at 56 ± 21 nm but has a width. Such distribution of particles may require different pump fluencies to undergo the transition due to, e.g., differences in band structure and optical absorption length. Additionally, we must consider polarization effects. After passing the $\lambda/2$ plate and Glan−Thomson polarizer, the laser pump pulse of the microscope is polarized. The electronic excitation probability depends on the alignment of the laser electric field and the transition moment of individual particles, and thus the dependence on particle size, orientation, and the density of states. In the monoclinic phase, the $V^{4+}-V^{4+}$ dimers have their bond oriented along the rutile *c* axis (see Figure 4), and one expects, because of polarization-dependent absorption, that some crystallites will be favorably excited even if all particles are randomly distrib-

uted. Details of polarization and particle size dependencies are the subject of future work.

Third, for the material studied, the time scale for the insulator to metal transition is ultrafast; see Figures 2 and 3. It follows that the transition is induced through optical excitation of carriers and not thermally through spatially separated nucleation sites and subsequent growth.[18] This observation is consistent with the fact that, at our fluence, the temperature rise is less than 1 K,[19] obtained from knowledge of the fluence and heat capacity;[15,20] if the transition is thermally induced, the drop in diffraction intensity would correspond to ~4 K (see ref 4). Several points are worth mentioning here. A 70 fs phase transition has been reported, from studies by optical reflection spectroscopy, and that this time scale changes to a few picoseconds if the sample thickness becomes relatively large.[7] Also, the "threshold" fluence depends on the sample, reducing to the value of 0.3 mJ/cm^2 for nanocrystals.[9] It is important to realize that changes in optical reflectivity do not directly reflect the actual structural transformation which involves bonding changes, nonequilibrium nuclear rearrangements, and possibly dislocations. The "threshold", besides extent of excitation, must depend on particle size, sample quality, and the initial temperature of the material on the hysteresis curve; our fluence and sample condition are similar to those of Kim et al.[10] As discussed elsewhere,[21] femtosecond excitation of a semiconductor through carriers involves two subsystems of the electrons and lattice, and electron−phonon coupling takes place in a few picoseconds. Thus, the transition to the metallic phase involves metastable state(s).

Finally, fourth, the relaxation (recovery) of the metallic phase takes for our material about 1 ns. Considering that the laser spot size on the thin film is ~50 μm, lateral heat diffusion is expected to take place on the μs or longer time scale; given the absorption coefficient (8×10^{-3} nm^{-1}),[20] the sample, which is not on a substrate, is uniformly excited in the z direction, and diffusion in this direction is not possible. However, given the imaging geometry, carrier diffusion within the material is a much faster process. In the presence of the femtosecond laser excitation, some of the nanocrystallites (NC), originally in the insulator phase, turn into the metallic phase depending on the fluence of the femtosecond pulse. The higher the fluence the larger the probability for NCs to turn into the metallic phase, but saturation becomes the limiting value.

We developed the following simple model in order to account for the experimental temporal changes in a *distribution of nanoparticles*. Because the material film thickness is close to the diameter of the NCs, carrier diffusion is essentially a two-dimensional (2D) process. For carriers, the effective diffusion constant depends phenomenologically on laser fluence in that its effective value is given by the "in-particle" and bulk "metallic-type" diffusion constants, with the latter multiplied by the fraction of particles excited. The carriers generated by the laser have a larger effective diffusion constant if more NCs become metallic at higher fluences. This is because of the better connectivity in metallic grains. At very low fluences, however, the lower density of

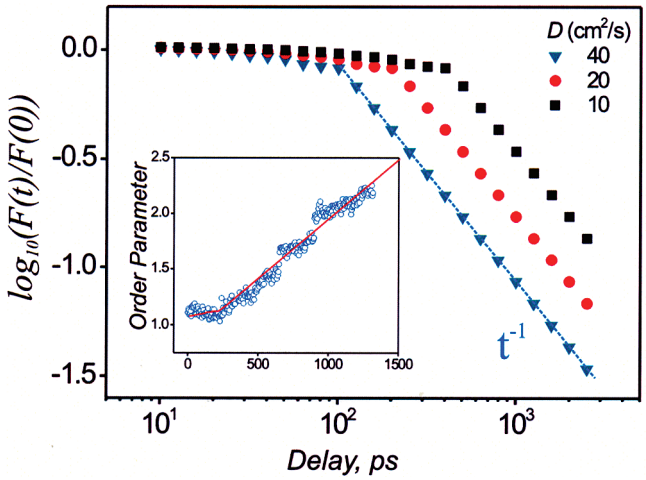

Figure 5. Theoretical and experimental results. The curves (log−log plot) for the normalized survival probability $F(t)$ are shown for different diffusion constants D and displays an initial plateau, reflecting connectivity among particles excited, and a long-time decay of t^{-1}, which is a characteristic of 2D diffusion. The inset gives the temporal behavior for the recovery of the order parameter with a fit for $D = 20$ cm^2/s. However, as discussed in the text, this value can be smaller by an order of magnitude if diffusion is within an e-probed zone.

the NCs in the metallic phase reduces the connectivity of the film and causes the effective diffusion constant to reach that of the in-particle value. Such a picture can explain the observation of an ultrafast decay in optical reflectivity, as hot carriers rapidly diffuse away, and also the fact that the recovery appears faster as the fluence increases.[11,12]

As shown in Figure 3, the order parameter $\eta(t)$ first changes in 3 ps, and this change is followed by a plateau and then a monotonic decrease. The order parameter,[18] which is a measure of the gradual change in the symmetry breaking process, is defined here to relate to the change of the total integrated intensity of a specific diffraction peak from the highest value (monoclinic) to the lowest one (rutile) as the phase changes. According to our model, the ultrafast phase transition leads to a metastable state in which metallic NCs within the e-beam radiation zone remain essentially unchanged for a finite time but then return to their initial state. The probability distribution of metallic NCs induced by the laser is similar to the spatial profile of the laser pulse on the sample film. We shall assume a Gaussian profile with a second moment distribution σ^2. The electron beam has a circular profile with a radius R (see Figure 4).

To calculate the survival probability of the photoinduced metallic NCs within the probed zone of an e-beam, we define $\rho(X,Y;t)$ as the density distribution of metallic NCs, for any X,Y distances, which follows the 2D diffusion equation:

$$\frac{\partial}{\partial t}\rho(X,Y;t) = D\left(\frac{\partial^2}{\partial X^2} + \frac{\partial^2}{\partial Y^2}\right)\rho(X,Y;t) \qquad (1)$$

Using the Green's function method, one can calculate $\rho(X,Y;t)$ at a later time t, knowing the initial value at $t = 0$:

$$\rho(X,Y;t) = \int_{-W/2}^{W/2} dx \int_{-W/2}^{W/2} dy\, G(X,Y,x,y;t)\, \rho(x,y;0) \quad (2a)$$

where

$$\rho(x,y;0) = \frac{1}{2\pi\sigma^2} \exp(-(x^2 + y^2)/2\,\sigma^2) \quad (2b)$$

The double integration is over the laser-irradiated sample region (defined by x,y) with a width W. The 2D Green's function in the above equation is defined as:

$$G(X,Y,x,y;t) = \frac{1}{4\pi Dt} \exp\left(-\frac{(X-x)^2 + (Y-y)^2}{4Dt}\right) \quad (2c)$$

The experimental observable, which is the survival probability, $F(t)$, of these photoinduced metallic NCs within the e-beam zone can now be calculated:

$$F(t) = \int_0^R r\, dr \int_0^{2\pi} d\theta\, \rho(r, \theta;t) \quad (3)$$

The integration is over the circular zone, with R being the radius of the e-region and $X = r \cos \theta$ and $Y = r \sin \theta$ the polar coordinates. The numerical integration is straightforward and here was performed with 5000 lattice points for each coordinate.

In Figure 5, the theoretical curves shown are the numerical solution of eq 3 for different D values. The best fit gives $D = 20$ cm^2/s at the fluence used if diffusion is to regions outside the electron zone area; if within, D becomes much less in magnitude (0.2−2 cm^2/s). The obtained values are significantly larger than that of heat diffusion in VO_2 ($D_{heat} \approx 0.02$ cm^2/s[15,19]) but close to the carrier diffusion value we calculated from mobility measurements ($D \sim 0.2$ cm^2/s[15]); for semiconductors,[22] D reaches about 20 cm^2/s, while for metals, say, gold, $D \sim 150$ cm^2/s.[23] We note that the diffusion in 2D gives dependence (t^{-1}) that is different from that of one-dimensional (1D) ($t^{-1/2}$) or three-dimensional (3D) ($t^{-3/2}$) diffusion. At high fluencies and/or for large D values, the plateau shrinks and the apparent recovery appears faster.

Given these observations, it is relevant to discuss structural dynamics in relation to band structure and bonding. At the energy used (~1.6 eV) to create carriers, only the electrons of the $3d_{||}$-band are available for excitation. The V^{4+} ions have a single electron in the $3d_{||}$-band, and this electron is responsible for the bonding of the V−V pairs and the quenching of the metallic state in the monoclinic structure.[24] The dimerization, antiferroelectric distortion of the VO_6 octahedron, and electron correlation effects all contribute significantly to the electronic band structure.[25] Thus, the localized 3d electrons, confined in the homopolar V^{4+}−V^{4+} bonds, are promoted into the delocalized conduction band and this process relieves the quenching of the metallic character. The change in electronic structure results in the movements of atoms in a rutile-like potential, with essentially no barrier, toward the new equilibrium position of a higher symmetry (see Figure 4). As a consequence, a metastable rutile-like structure is formed, but final domains of the new phase will form depending on the density of carriers and the material. From the hysteresis behaviors,[4] the abrupt change in the percentage of rutile concentration at the initial temperature means that the formed new phase, when electron−hole carriers decay, will acquire back the initial phase at the same temperature.

The fluence used here (~0.1 mJ/cm^2) is similar to that employed in a recent study by Kim et al.[10] (see change in transmission with time in Figure 1a of ref 10), indicating that a critical carrier excitation is essential for inducing the ultrafast change and that relatively high fluencies are for saturation of the whole ensemble. The total carrier density required is the sum of the thermal and photoinduced one. Moreover, their results, using coherent phonon analysis, are consistent with presence of the metastable nonequilibrium structure discussed above. It appears that the motion is driven by potential changes rather than directly through phonons. The V atoms would have to move a distance of ~0.2 Å and such a displacement is close to the Lindemann limit for melting (10% of a closest nearest-neighbor distance).[14,26] Absent from this picture is consideration of dislocations, crystallite size distribution, and material physical properties. In a forthcoming publication, we will report results of the transition in the high fluence regime, resolving both the picosecond and femtosecond dynamics with Bragg diffraction.

In conclusion, we have demonstrated the direct imaging of structural dynamics during a phase transition. The transition is followed both in real and Fourier space. The critical role of the carriers in driving the structural change and the distinction between electronic redistribution and nuclear rearrangement define the nature of the first-order phase transition. For strongly correlated systems, these carriers, which result from thermal, chemical, and photon doping,[3] assist in the reduction of the on-site Coulomb energy of a Mott insulator.[10] It follows that understanding the true nature of the transition requires spatial and temporal resolutions of the metastable changes of microscopic order (symmetry and unit cell) and those of macroscopic properties (morphology, grain structure, particle size). UEM, which offers such resolutions, is now poised to further examine this system and also a variety of other nanostructured materials undergoing unique correlated transformations.[3,27,28] Such studies, including those of biological systems, are the main focus of the Physical Biology Center for Ultrafast Science and Technology at Caltech.

Acknowledgment. This research was supported by the Gordon and Betty Moore Foundation, the National Science Foundation, and the Air Force Office of Scientific Research. J.W. gratefully acknowledges partial support from the Knut and Alice Wallenberg foundation.

References

(1) Zewail, A. H. *Annu. Rev. Phys. Chem.* **2006**, *57*, 65 and references therein.
(2) Thomas, J. M. *Angew. Chem., Int. Ed.* **2005**, *44*, 5563.
(3) Gedik, N.; Yang, D. S.; Logvenov, G.; Bozovic, I.; Zewail, A. H. *Science* **2007**, *316*, 425.

(4) Grinolds, M. S.; Lobastov, V. A.; Weissenrieder, J.; Zewail, A. H. *Proc. Natl. Acad. Sci. U.S.A.* **2006**, *103*, 18427.
(5) Lobastov, V. A.; Srinivasan, R.; Zewail, A. H. *Proc. Natl. Acad. Sci. U.S.A.* **2005**, *102*, 7069.
(6) Zewail, A.; Lobastov, V. Method and system for ultrafast photoelectron microscope. US 7,154,091 B2, 20050401, 2006.
(7) Cavalleri, A.; Chong, H. H. W.; Fourmaux, S.; Glover, T. E.; Heimann, P. A.; Kieffer, J. C.; Mun, B. S.; Padmore, H. A.; Schoenlein, R. W. *Phys. Rev. B* **2004**, *69*, 153106.
(8) Cavalleri, A.; Dekorsy, T.; Chong, H. H. W.; Kieffer, J. C.; Schoenlein, R. W. *Phys. Rev. B* **2004**, *70*, 161102.
(9) Cavalleri, A.; Rini, M.; Schoenlein, R. W. *J. Phys. Soc. Jpn.* **2006**, *75*, 9 and references therein.
(10) Kim, H. T.; Lee, Y. W.; Kim, B. J.; Chae, B. G.; Yun, S. J.; Kang, K. Y.; Han, K. J.; Yee, K. J.; Lim, Y. S. *Phys. Rev. Lett.* **2006**, *97*, 266401.
(11) Lysenko, S.; Rua, A. J.; Vikhnin, V.; Jimenez, J.; Fernandez, F.; Liu, H. *Appl. Surf. Sci.* **2006**, *252*, 5512.
(12) Vikhnin, V. S.; Lysenko, S.; Rua, A.; Fernandez, F.; Liu, H. *Solid State Commun.* **2006**, *137*, 615.
(13) Pan, M.; Zhong, H. M.; Wang, S. W.; Liu, J.; Li, Z. F.; Chen, X. S.; Lu, W. *J. Cryst. Growth* **2004**, *265*, 121.
(14) Rogers, K. D. *Powder Diffr.* **1993**, *8*, 240.
(15) Berglund, C. N.; Guggenheim, H. J. *Phys. Rev.* **1969**, *185*, 1022.
(16) Parkin, I. P.; Manning, T. D. *J. Chem. Educ.* **2006**, *83*, 393.
(17) Eyert, V. *Ann. Phys. (Berlin)* **2002**, *11*, 650.
(18) Landau, L. D.; Lifshits, E. M. *Statistical Physics; Course of Theoretical Physics, Vol. 5*, 2nd ed.; Pergamon: New York, 1968.
(19) Using a heat capacity of 60 J/molK,[15] and knowing the molar mass of 82.9 g/mol (atomic weight), the density of 4.3 g/cm^3, the volume, and the pulse fluence at the sample and the absorption coefficient of 0.008 nm^{-1},[20] we obtained <1 K. The heat diffusion constant (D = 0.02 cm^2/s) was calculated from the thermal conductivity (70 mW/cmK[15]), density, and specific heat capacity (heat capacity/molar mass).
(20) Kakiuchida, H.; Jin, P.; Nakao, S.; Tazawa, M. *Jpn. J. Appl. Phys.* **2007**, *46*, L113.
(21) Yang, D. S.; Gedik, N.; Zewail, A. H. *J. Phys. Chem. C* **2007**, *111*, 4889.
(22) Kunst, M.; Grunow, P. *Sol. Energy Mater. Sol. Cells* **2004**, *83*, 409.
(23) Hohlfeld, J.; Wellershoff, S. S.; Gudde, J.; Conrad, U.; Jahnke, V.; Matthias, E. *Chem. Phys.* **2000**, *251*, 237.
(24) Goodenough, J. B. *J. Solid State Chem.* **1971**, *3*, 490.
(25) Laad, M. S.; Craco, L.; Muller-Hartmann, E. *Phys. Rev. B* **2006**, 73.
(26) Lindemann, F. A. *Phys. Z.* **1910**, *11*, 609.
(27) Jacobs, K.; Zaziski, D.; Scher, E. C.; Herhold, A. B.; Alivisatos, A. P. *Science* **2001**, *293*, 1803.
(28) Eskildsen, M. R.; Gammel, P. L.; Barber, B. P.; Yaron, U.; Ramirez, A. P.; Huse, D. A.; Bishop, D. J.; Bolle, C.; Lieber, C. M.; Oxx, S.; Sridhar, S.; Andersen, N. H.; Mortensen, K.; Canfield, P. C. *Phys. Rev. Lett.* **1997**, *78*, 1968.

NL071341E